Shap. Mem. Superelasticity
https://doi.org/10.1007/s40830-024-00476-y

ORIGINAL RESEARCH ARTICLE

Evaluation of Thermomechanical Properties in a 2D Rotational Elastocaloric Prototype: A Numerical Study for Enhanced Energy Efficiency

Luca Cirillo[1] · Adriana Greco[1] · Claudia Masselli[1]

Received: 12 October 2023 / Revised: 21 November 2023 / Accepted: 30 January 2024

Abstract So far, much of the research on the caloric effect has focused on the magnetocaloric effect, which was the first investigated chronologically, in the field of room temperature for about 40 years. Subsequently and especially in the last decade, scientific research has focused on the development of solid-state technologies other than the magnetocaloric one, including the one of interest for this work: elastocaloric technology. This work is part of the "SUSSTAINEBLE" project of the Department of Industrial Engineering at the University Federico II of Naples, aimed at developing the first Italian prototype of an elastocaloric device for environmental conditioning. The prototype is currently in the experimental development phase and its design and construction are dynamically accompanied by a two-dimensional numerical model that fully reproduces its thermo-fluid dynamic operation. The rotary-type prototype consists of 600 Nickel Titanium wires subjected to loading and unloading phases controlled by a properly programmed optical encoder. The thermo-fluidic medium that regulates heat transfer is air. The aim is to characterize the operation of the elastocaloric device using numerical analysis software in order to optimize its geometric, operational, and environmental parameters, to maximize its energy performance in terms of temperature difference, useful thermal power, and coefficient of performance.

This invited article is part of a special topical focus in *Shape Memory and Superelasticity* on Elastocaloric Effects in Shape Memory Alloys. The issue was organized by Stefan Seelecke and Paul Motzki, Saarland University.

✉ Adriana Greco
adriana.greco@unina.it; adrgreco@unina.it

[1] Department of Industrial Engineering, DII, University of Naples Federico II, Piazzale Tecchio 80, 80125 Napoli, Italy

Keywords 2D model · Numerical analysis · Caloric effects · Active elastocaloric regenerative refrigeration cycle

List of Symbols

Roman Symbols

A	Austenite phase temperature, K
B	Boltzmann constant, m^2 kg s^{-2} K^{-1}
C	Coefficient of K-$\hat{\varepsilon}$ model
C	Specific heat capacity, J kg^{-1} K^{-1}
CO_2	Emissions of equivalent carbon dioxide, kg
COP	Coefficient Of Performance, -
D	Diameter, mm
E	Energy, J
$\bar{E}$	Young modulus, MPa
f	Frequency, Hz
g'''	ElastoCaloric term, W m^{-3}
Gr	Grashof number, -
H	Latent heat, J g^{-1}
h	Convective coefficient, W m^{-2} K^{-1}
$\vec{I}$	Identity vector, -
K	Turbulent kinetic energy, J
k	Thermal conductivity, W m^{-1} K^{-1}
L	Length of the wire, mm
Nu	Nusselt number, -
p	Pressure, Pa
Pr	Prandtl number, -
$\dot{Q}$	Thermal power, W
RC	Refrigerant charge, kg
s	Entropy, J kg^{-1} K^{-1}
T	Temperature, K
t	Time, s
V	Volume, m^3
$\vec{v}$	Velocity vector, m s^{-1}

Published online: 22 March 2024

w	Loading/unloading work, J g^{-1}
x	Longitudinal spatial coordinate, m
y	Orthogonal spatial coordinate, m

Greek Symbols

Δ	Finite difference
δ	Percentage rate of refrigerant, % yr^{-1}
ε	Strain, N
$\hat{\varepsilon}$	Turbulent cinematic viscosity, m^2 s^{-1}
θ	Transformation relaxation time constant, s
ξ	Phase fraction, -
$\dot{\xi}$	Instantaneous phase fraction, s^{-1}
μ	Dynamic viscosity, Pa s^{-1}
ρ	Density, kg m^{-3}
σ	Uniaxial stress, MPa
τ	Tangential stress, Pa m^{-1}
ψ	Probability,

Subscripts

A	Austenitic
AM	Austenite-to-Martensite transformation
ad	Adiabatic
air	Air
cool	Cooling mode
dir	Direct
eff	Effective
env	Environment
f	Finish
hot	Heat pump operation mode
ind	Indirect
inlet	Inlet
is	Isothermal
L	Annual refrigerant regular leak
M	Martensitic
MA	Martensite-to-Austenite transformation
mat	Material
p	Constant pressure
R	Refrigerant leak related to dismission
ref	Refrigeration
SMA	Shape Memory Alloy
span	Span
T	Constant temperature
t	Turbulent
V	Useful life of the system

Acronyms

A	Austenitic
AC	Air Conditioning
AeR	Active elastocaloric Regenerative refrigeration
eCE	ElastoCaloric Effect
GWP	Global Warming Potential
HCFC	HydroChloroFluoroCarbon
HFC	HydroFluoroCarbon
HFO	HydroFluoroOlefins
HVAC	Heating Ventilating & Air Conditioning
M	Martensitic
MCE	MagnetoCaloric Effect
ODP	Ozone Depletion Potential
SMA	Shape Memory Alloy
TEWI	Total Equivalent Warming Impact

Introduction

Refrigeration and environmental control have become indispensable elements of modern living and the global economy. They are now firmly integrated into various sectors, such as building regulation, food retail, healthcare, and manufacturing. In 2010, residential air conditioning accounted for just 10% of global electricity demand, but it is expected to rise to 30% by 2040. This surge in energy consumption underscores the urgency of implementing energy policies that enhance building energy efficiency and encourage the adoption of more efficient air conditioning technologies, with the aim of reducing energy usage and emissions for a greener and more sustainable future. In this context, research efforts are increasingly shifting toward exploring alternatives to conventional vapor compression systems, with a particular emphasis on solid-state devices utilizing the caloric effect [1, 2]. Historically, much of the research on the caloric effect has centered on the magnetocaloric effect, which has been investigated for approximately four decades in room-temperature applications [3]. However, in recent years, scientific research has expanded beyond the magnetocaloric effect, leading to the development of various solid-state technologies. One such technology, which is the focus of this work, is elastocaloric technology [4–7]. Elastocaloric effects occur when external mechanical forces are applied and removed from specific materials known as shape memory alloys (SMAs). This results in either a change in temperature within the materials under adiabatic conditions or an alteration in entropy due to variations in the intensity of the applied field under isothermal conditions.

In recent times, there have been numerous prototypes developed and examined, focusing on harnessing the elastocaloric effect. These prototypes can be categorized and segmented based on four key parameters: the device's fundamental concept, the method of heat transfer, the type of mechanical load applied, and the specific elastocaloric material used (referred to as eCM). Additionally, these various devices can be classified based on the type of cycle they employ and whether or not they incorporate a process known as regeneration [8]. Regeneration is employed to ensure that a device can achieve temperature intervals (ΔTspan) that surpass the intrinsic temperature change capacity (ΔTad) of the materials involved [9]. Specifically, there are three

distinct approaches to achieving this: active regeneration, cascade architecture [10], and heat recovery. In this review of the current state of the field, our primary focus is on prototypes falling within the second category, as our aim is to create a device that operates on a macro-scale. Within an elastocaloric device, heat transfer can take place either through conduction (referred to as Solid-to-Solid Heat Transfer—SSHT) or through convective heat exchange between the elastocaloric material and the heat transfer fluid (HTF), typically consisting of water or air. Furthermore, these devices can be categorized based on the relative motion between the elastocaloric material, the heat transfer fluid, and the heat exchangers. Specifically, these devices can be entirely stationary, meaning there is no movement involved in regulating heat transfer. Alternatively, in the absence of a heat transfer fluid, the elastocaloric material (eCM) can be mobile, while the heat exchangers remain stationary or the elastocaloric material can remain stationary while the heat exchangers move. It is also possible for both the elastocaloric material and the heat exchangers to be in motion simultaneously. The configuration that lacks relative motion can only operate when paired with thermal diodes [11]. In this arrangement, heat transfer is regulated through conductive interaction involving a material that can modify its thermal conductivity depending on the intensity of an external field applied. Additionally, this setup offers enhanced efficiency compared to the previously examined cycles, as it enables the optimization of heat exchange between the two materials.

Moreover, devices can be further categorized based on the motion of their primary actuator, which can be linear or continuously rotary. They can also be segmented based on the type of stress applied to the elastocaloric material (eCM). Specifically, this stress may take the form of tension or compression [12, 13], although torsion [14] or bending [15] can also be applied. In thin geometries, tension stresses can be applied through out-of-plane deflections.

Finally, elastocaloric refrigeration systems can be further categorized based on the selection of the eCM employed as the active element within the apparatus [16]. At present, NiTi-based SMAs are the dominant choice for eCMs. Common shapes include films, wires, plates, or tubes, although more intricate configurations are also utilized. The most recent prototype in this field, introduced by Qian et al. [9] in May 2023, offers a temperature interval range (ΔT_{span}) of up to 22.5 K and can achieve refrigeration power levels of up to 260 W. A notable feature of this system, which comprises four bundles of 19 NiTi tubes (paired in twos to reduce the mechanical effort needed for elastocaloric effect implementation), is its high versatility. By simply controlling the operational sequence and manipulating appropriate valves in the heat transfer fluid network (usually water), the device can function in both active regeneration mode (maximizing ΔT) and maximum utilization mode (optimizing exchanged refrigeration power); this is termed "multimode" operation. Another significant aspect is the application of uniaxial stress to the SMA tubes, involving compression through actuators. While this type of stress can generate a similar elastocaloric effect as tension, it mitigates the formation of microfractures, significantly extending the lifespan of the SMA alloy to over 10 million cycles. To ensure robust mechanical strength and maximize thermal exchange efficiency between the SMA and water, the prototype is designed with a hexagonal configuration, with each bundle of tubes encased by a layer of 18 stainless steel tubes. This arrangement not only prevents direct contact of the NiTi with the outer supporting wall but also maintains structural stability. To further enhance thermal exchange efficiency between the fluid and the NiTi tubes through which it flows, triangular polymeric inserts are positioned inside each tube.

For brevity, a summary table (Table 1) is provided below, encapsulating the current state of elastocaloric prototypes for refrigeration or environmental control, as documented in the literature, along with their key characteristics. The study of solid-state refrigeration devices employing the elastocaloric effect has been ongoing for more than a decade, resulting in the development of approximately fifteen laboratory-designed elastocaloric devices, with the most significant ones detailed in the preceding section.

Most of the numerical and mathematical models developed and presented to the scientific community for these prototypes are one-dimensional (1D), although more complex and detailed models also exist. These models can be divided into three main categories:

- Elastocaloric effect models—These models describe the physical phenomena and processes leading to the manifestation of the elastocaloric effect in the material: an increase in temperature following loading and the occurrence of the austenite-to-martensite transformation, as well as a decrease in temperature in the case of the MA transformation [17–19]. These models are useful in evaluating and optimizing elastocaloric materials for use in refrigeration devices.
- Numerical models of elastocaloric devices—They describe the operation of elastocaloric devices by analyzing not only the elastocaloric effect but also heat transfer phenomena to assess the energy performance of these devices [20].
- Thermodynamic models—These models define the thermodynamic cycle that occurs within the device and can be used to predict the efficiency and cooling capacity of the cycle.

In a review conducted by Silva et al. [1] in 2021, the primary focus was on numerical models that had been

Table 1 List of experimental prototypes developed and found in the literature

Type	Stress	eCM	Cycle	HTF	ΔT_{span} [K]	Q_{cool} [W]	SCP [W/g]	COP [-]	Year	Authors	References
Wire	Traction	NiTi	AeR	Air	25,5	-	-	2,7	2012	Cui et al	[24]
D = 0,5 mm	Compression				17	-	-	3,05			
Plate	Traction	$Ni_{50,8}$ $Ti_{49,2}$	Solid–Solid	-	7	-	0,35	4,65	2015	Schmidt et al	[25]
L = 90 mm											
W = 3,2 mm											
s = 0,5 mm											
Tube	Compression	NiTi	AeR	Water	-	65	0,13	-	2015	Qian et al	[26]
L = 25,54 cm											
D_e = 5 mm											
s = 0,5 mm											
Foil	Bending	NiTi	Solid–Solid	-	3,5	20 10^{-3}	-	3	2015	Ossmer et al	[27]
Area = 20mm^2											
Tube	Latent heat exchange	NiTi	AeR	Water	5,6	7,9	6,27	-	2016	Fraunhofer IPM	[28]
Plate	Traction	$Ni_{55,8}$ $Ti_{44,2}$	AeR	Water	15,3	0,703	0,782	5	2017	Tusek	[29]
L = 50 mm											
W = 10 mm											
s = 0,2 mm											
Foil	Bending	$Ni_{50,5}$ $Ti_{49,1}Fe_{0,4}$	Solido-Solido	-	9,4	-	7,7	3,1	2018	Ossmer et al	[30]
L = 15 mm											
W = 2 mm											
s = 0,03 mm											
Wire	Traction	$Ti_{55,2}$ $Ni_{29,3}$ $Cu_{12,7}$ $Co_{2,8}$	AeR	Air	20	250	0,922	9,5	2018	Kirsch et al	[31]
L = 300 mm											
D = 0,2 mm											
Fili	Flessional	NiTi	Solid–Solid	Aria	1,3	30 10^{-3}	-	1,38	2019	Sharar et al	[32]
								2,55			
Films	Bending	TiNiCu Co	Solid-Solido	-	7,6	0,145	6,245	1,9	2019	Bruderlin et al	[33]
L = 20 mm					-			-			
W = 2 mm											
s = 30 µm					15			5,7			
Wire	Traction	NiTi, CuZ, CoTi	Multimode	Water	28,3	-	0,042	7,7	2020	Snodgrass et al	[34]
D = 1,27 mm											
Wire	Traction	Rubber	AeR	Air	1,2	-	-	-	2020	Sebald et al	[35]
D_e = 5 mm											
L = 25 mm											

Table 1 (continued)

Type	Stress	eCM	Cycle	HTF	ΔT_{span} [K]	Q_{cool} [W]	SCP [W/g]	COP [-]	Year	Authors	References
Wire	Traction	NiTi	AeR	Air	9,2	3,1	0,34	-	2022	Chen et al	[36]
Foil	Flessional	$Ni_{56}Ti_{44}$	AeR	Air	-	11,5	0,137	-	2022	Cheng et al	[37]
L = 100 mm											
W = 25 mm											
s = 0,5 mm											
Tube	Compression	$Ni_{56,25}$ $Ti_{43,75}$	AeR	Air	5	1,5	1,071	-	2022	Ianniciello et al	[38]
H = 9 mm											
D_e = 2,40 mm											
D_i = 1,76 mm											
Tube	Compression	NiTi	Multimode	Air	22,5	0	0	-	2023	Qian et al	[9]
L = 254 mm											
D_e = 4,724 mm					1,9	260	0,324	1,03/6,85			
Di = 3,759 mm											

introduced to the scientific community up until the year 2020, specifically concerning devices utilizing caloric effects. Since 2010, there has been a significant exponential rise in the number of publications related to caloric effects, with the majority of them revolving around magnetocaloric and electrocaloric effects. It was only in the past decade that attention began to shift toward caloric effects induced by changes in pressure or mechanical stress, such as barocaloric and elastocaloric effects. The authors of the review noted that the majority of these numerical models shared with the scientific community were one-dimensional (1D) and primarily geared toward the development of large-scale devices. Starting from 2022, Cirillo et al. [21] initiated the development of a two-dimensional (2D) model for the creation of an elastocaloric refrigerator prototype. This rotating 2D model enabled the identification of fluid dynamic challenges that impacted the temperatures at the output of the prototype. Up to that point, their analysis had focused on constant external conditions [20, 22]. In the present study, the same authors aimed to conduct numerical testing to assess the optimal conditions of the device as the applied thermal load varies. It is worth noting that this model is the sole 2D rotary model documented in the literature.

The Italian Prototype and Numerical Model

The project involved designing a device that allows exploring its functionality through testing in various configurations, aimed at investigating the feasibility of the elastocaloric effect for room-temperature refrigeration applications.

The secondary fluid aeraulic system of the device consists of

- Control valves to regulate the flow direction;
- Fans to ensure adequate flow rates ranging from 10 to 200 m^3/h;
- Elastocaloric material composed of $Ni_{50.8}Ti_{49.2}$ wires with a diameter of 0.50 mm and a length of 300 mm;
- Sensors and devices for measuring pressure, temperature, and velocity.

As illustrated in Fig. 1, the apparatus is composed of two concentric cylinders, with diameters measuring 280 and 250 mm and lengths extending to 300 mm. These cylinders facilitate the flow of air within them. The airflow interacts perpendicularly with the elastocaloric material wires, which amount to a total of 600 wires, as depicted in Fig. 1a. To manage the loading and unloading phases of the cycle, these elastocaloric material wires are linked to ten hydraulic cylinders that rotate. These cylinders are paired together to ensure the recovery of expansion work. At the core of the equipment lies the AeR regenerator (Active elastocaloric

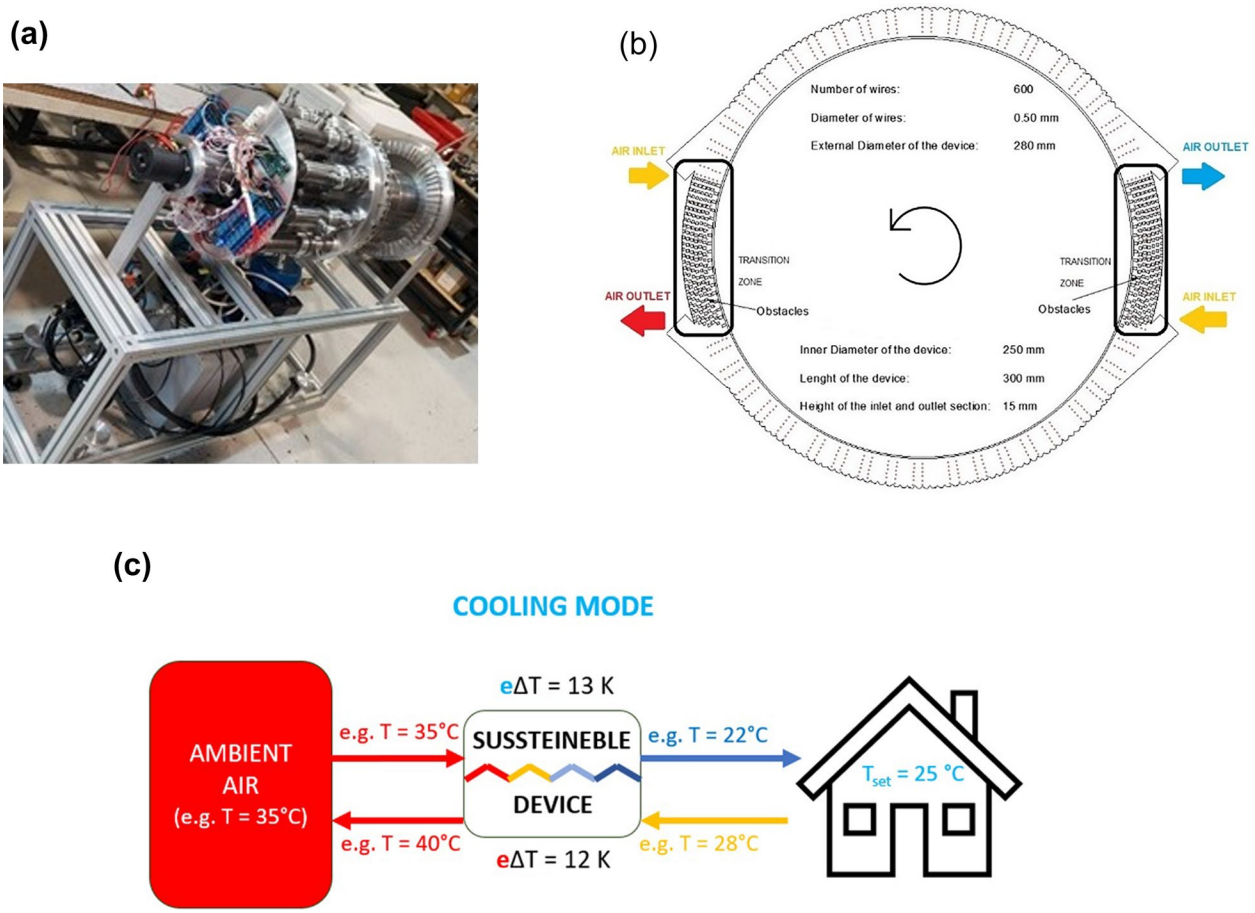

Fig. 1 The Italian Prototype: **a** Pic of the prototype under construction; **b** 2D of prototype section; **c** Functioning details and principle of the device

Regenerative refrigeration cycle), which incorporates NiTi wires of elastocaloric material encased within an aluminum housing. This solution is adopted for the following purposes:

- Accommodate the deformation of the elastocaloric material in response to the loading (tension) operation;
- Ensure thermal isolation of the regenerator from the external environment.

At the extremities of the device, fans are strategically positioned within the outlet channels to facilitate air movement. The apparatus incorporates two regenerators: one hot and one cold. Each of these regenerators occupies a substantial portion of the circular arrangement, excluding the transitional zones between the air inlet and outlet channels. In the cold regenerator, ambient temperature air enters and interacts with the cold wires, resulting in the production of cold air (used for cooling purposes in summer conditioning) due to the elastocaloric effect during unloading. Conversely, in the hot regenerator, ambient temperature air enters and encounters the hot wires, generating hot air for use in winter conditioning (in the operation of a heat pump) as a result of the elastocaloric effect during loading. To enhance heat exchange between the elastocaloric material and air, both internal and external promoters are employed. These promoters not only improve heat transfer efficiency but also prevent the air from adhering flatly to the outer surface of the cylinder, a phenomenon caused by the centrifugal force generated by the device's rotation. This design keeps the airflow separated from the external surface, promoting efficient heat exchange with the elastocaloric material. The inclusion of hydraulic pistons ensures that the wire pulling operation, crucial for the occurrence of the elastocaloric effect, occurs in a manner parallel to the direction in which the material deforms (resulting in linear deformation), thereby minimizing friction. Specifically, for work recovery purposes, the ten pistons are paired up so that mechanical power is utilized just once to actuate them. In practice, while one piston is loading, the other is unloading, ensuring energy recovery. This approach serves to maximize system efficiency and minimize energy wastage. The prototype is intentionally designed with the flexibility to vary several key aspects:

- The choice of elastocaloric material to be used.
- The geometry of the elastocaloric material.
- The arrangement of the channels.

This adaptability allows for the testing of different design configurations to determine the optimal one in terms of energy performance. The preliminary design of the prototype encompasses multiple phases, including requirements definition, modeling, and simulation.

The Numerical Modeling

The rotary elastocaloric prototype under consideration comprises a circular arrangement of 600 SMA wires made of $Ni_{55.92}Ti_{44.08}$ alloy. This circular setup is configured with two inlets and two outlets, which can be utilized concurrently for both cooling and heat pump functions. Air is introduced through these inlets and flows through the SMA wires. The elastic deformation of the SMA wires absorbs or releases heat energy from the air, resulting in either cooling or heating effects, depending on the thermodynamic cycle employed. Crucially, the rotary elastocaloric prototype is engineered to operate without the need for heat exchangers, thereby reducing system costs and complexity. The rotation frequency can vary between 0.3 and 0.7 Hz, while air velocity can range from 3 to 20 m per second. These attributes enable the system to adapt effectively to diverse environmental conditions, ensuring flexibility and efficiency. The choice of an outer diameter of 280 mm and an inner diameter of 250 mm for the circular arrangement was deliberate, as it guarantees ample contact surface between the SMA wires and the moving air, thereby maximizing the cooling or heating effect. Additionally, the outlet sections, measuring 15 mm in height and 300 mm in depth, are meticulously designed to promote uniform and controlled airflow, thereby minimizing pressure losses and optimizing the system's efficiency. To evaluate the device's efficiency and enhance its design, a numerical study was conducted. This study utilized commercial software, employing a numerical modeling approach to significantly reduce design timelines and costs through a comprehensive thermo-fluid dynamic analysis. To simplify the analysis process, some underlying assumptions were made to focus only on the prototype's key factors. In particular, it was assumed that

- the time required for the transition from the austenitic phase to the martensitic phase is negligible compared to the time required for heat exchange;
- the loading and unloading process occur axially to the wire;
- the outer walls of the prototype are considered adiabatic through an insulation layer to prevent heat dissipation during the refrigeration process. In other words, this assumption serves to ensure that there is no temperature variation outside the prototype, which could affect its efficiency;
- the austenite and martensite phase is uniform throughout the wire;
- the Navier–Stokes equations govern the temperature distribution of the fluid and solid due to convective heat transfer;
- the convective heat transfer is dominant compared to internal thermal conduction within the wire as the Biot number is less than 0.1

The Mathematical Description

According to the hypothesis of the physical domain the governing equations are the following:

–The continuity equation

$$\frac{\partial \rho}{\partial t} + \nabla\left(\rho \vec{u}\right) = 0 \tag{1}$$

–The momentum equation

$$\rho \frac{\partial \vec{u}}{\partial t} + \rho\left(\vec{u} \cdot \nabla\right)\vec{u} = \nabla \cdot \left\{ -p\vec{I} + \left(\mu + \mu_T\right)\left[\nabla \vec{u} + \left(\nabla \vec{u}\right)^T\right]\right\} \tag{2}$$

where μ_T is the turbulent viscosity defined as

$$\mu_T = \rho C_\mu \frac{K}{\hat{\varepsilon}} \tag{3}$$

With C_μ that is one of the constants of the K-$\hat{\varepsilon}$ model for turbulent flow.

–The energy equation

$$\frac{\partial(\rho E)}{\partial t} + \nabla\left[\vec{u}(\rho E + p)\right] = \nabla \cdot \left[k_{eff}\nabla T - \sum_j h_j \vec{J}_j + \left(\tau_{eff} \cdot \vec{u}\right)\right] \tag{4}$$

where k_{eff} is the effective conductivity defined as the sum of the conventional thermal conductivity of the fluid (k_f) and the thermal conductivity of the turbulent (k_T) and thus modeled as follows:

$$k_{eff} = k_f + k_T \tag{5}$$

Using the K-$\hat{\varepsilon}$ model for turbulent flow, the turbulence kinetic energy equation is as follows:

$$\frac{\partial(\rho K)}{\partial t} + \rho \vec{u} \cdot \nabla K = \nabla\left[\left(\mu + \frac{\mu_T}{\sigma_K}\right)\nabla K\right] + P_K - \rho\varepsilon \tag{6}$$

where P_K can be evaluated as follows:

$$P_K = \mu_T\left[\nabla \vec{u} : \left(\nabla \vec{u} + \left(\nabla \vec{u}\right)^T\right) - \frac{2}{3}\left(\nabla \cdot \vec{u}\right)^2\right] - \frac{2}{3}\rho K \nabla \cdot \vec{u} \tag{7}$$

The specific dissipation rate equation is as follows:

$$\frac{\partial(\rho\varepsilon)}{\partial t} + \rho \vec{u} \cdot \nabla \varepsilon = \nabla\left[\left(\mu + \frac{\mu_T}{\sigma_{\hat{\varepsilon}}}\right)\nabla \varepsilon\right] + C_{\hat{\varepsilon}1}\frac{\hat{\varepsilon}}{K}P_K - C_{\hat{\varepsilon}2}\rho\frac{\hat{\varepsilon}^2}{K} \tag{8}$$

Table 2 reports the experimental constants of the K-$\hat{\varepsilon}$ model.

The equation of the Energy of the SMA is as follows:

$$\frac{\partial T_{SMA}}{\partial t} = \frac{k_{SMA}}{\rho_{SMA} c_{SMA}} \left(\frac{\partial^2 T_{SMA}}{\partial x^2} + \frac{\partial^2 T_{SMA}}{\partial y^2} \right) + \dot{g}''' \tag{9}$$

where the power density $\dot{g}'''$ represents the elastocaloric effect and it is positive term during loading and negative during unloading, as reported in [23].

$$\dot{g}''' = \rho_{SMA}(\Delta H + w)\dot{\xi}_M \tag{10}$$

$\dot{g}'''$ is a power density [Wm^{-3}] that could be employed as a generation term in the energy equation of the solid refrigerant. The martensite volume fraction ξ_M is instantaneously estimated.

Boundary Conditions

The boundary conditions take into account the environmental conditions at the entrance both in terms of speed and temperature, while on the external and internal surface, the adiabatic condition is assumed:

–Adiabatic condition on the external and internal surface

$$-\vec{n} \cdot \vec{q} = 0 \tag{11}$$

–Inlet conditions

$$\vec{u} = -\vec{n} \cdot u_0$$

$$K = \frac{3}{2} u_0^2$$

$$\varepsilon = C_\mu^{\frac{3}{4}} \frac{K^{\frac{3}{2}}}{L_T}$$

$$T_{inlet} = T_{env} \tag{12}$$

–Outlet conditions

$$p_0 = 0$$

$$\nabla K \cdot \vec{n} = 0$$

$$\nabla \varepsilon \cdot \vec{n} = 0 \tag{13}$$

Table 2 Constants of the K-$\hat{\varepsilon}$ model

Constant	Value
C_μ	0.09
$C_{\hat{\varepsilon}1}$	1.44
$C_{\hat{\varepsilon}2}$	1.92

Operative Conditions

The ambient temperature (T_{inlet}), was fixed at 293 K, and the stress was applied or removed within 0.2 s (T_{load} and T_{unload}), at a rate of 0.25 s^{-1}, making the transformation adiabatic. The operating conditions for the simulations were optimized by adjusting the air velocity at the device inlet and the rotation frequency. The air velocity and the rotation frequency varied within a certain range, as shown in Table 3.

The thermal performances are evaluated in terms of temperature, cooling power, second-law efficiency, and COP, expressed by the following equations:

–Temperature variation on the cold side

$$\Delta T_{cold} = T_{air,in} - \frac{1}{t_{cycle}} \int_{0+n \cdot t_{cycle}}^{t_{cycle}+n \cdot t_{cycle}} T_{air,out,cold}(t) dt \tag{14}$$

–Temperature span variation

$$\Delta T_{span} = \frac{1}{t_{cycle}} \int_{0+n \cdot t_{cycle}}^{t_{cycle}+n \cdot t_{cycle}} \left(T_{air,out,hot} - T_{air,out,cold} \right) dt \tag{15}$$

–Cooling power

$$\dot{Q}_{cooling} = \frac{1}{t_{cycle}} \int_{0+n \cdot t_{cycle}}^{t_{cycle}+n \cdot t_{cycle}} \dot{m}_{air} c_{air} \left[T_{air,in} - T_{air,out,cold}(t) \right] dt \tag{16}$$

–Coefficient of Performance (COP)

$$COP_{cooling} = \frac{\dot{Q}_{cooling}}{\dot{W}} \tag{17}$$

where $\dot{W}$ is the mechanical work to apply the load (assuming a maximum work recovery) to the elastocaloric materials and to move the air in the circular crown ($\dot{W}_p$):

$$\dot{W}_P = \Delta P \cdot \dot{V}_{air} \tag{18}$$

where ΔP is the pressure drop into the circular crown and $\dot{V}_{air}$ is the volumetric rate of the air. While, the mechanical work consumed to rotate the wires is negligible because it is about two orders of magnitude lower than the other two components.

Results and Discussion

As the frequency increases, the point where the maximum temperature variation occurs shifts to the right side of the graph. This shift is driven by the fact that the maximum power that can be extracted also increases proportionally,

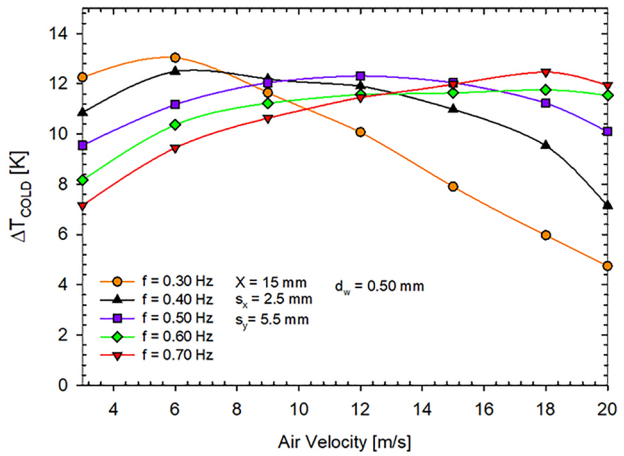

Fig. 2 Air temperature variation in the cold regenerator vs velocity parametrized for cycle frequency

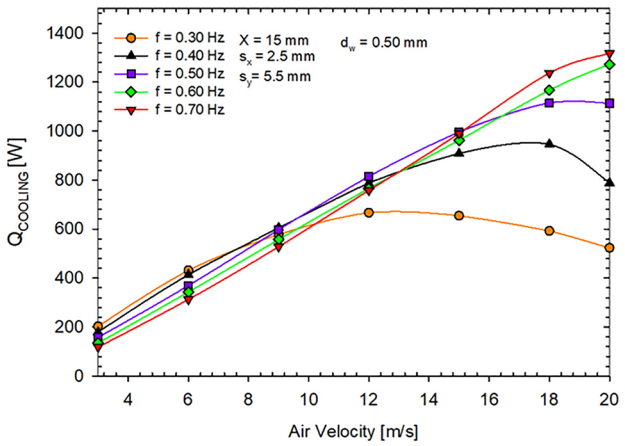

Fig. 3 Cooling power vs velocity parametrized for cycle frequency

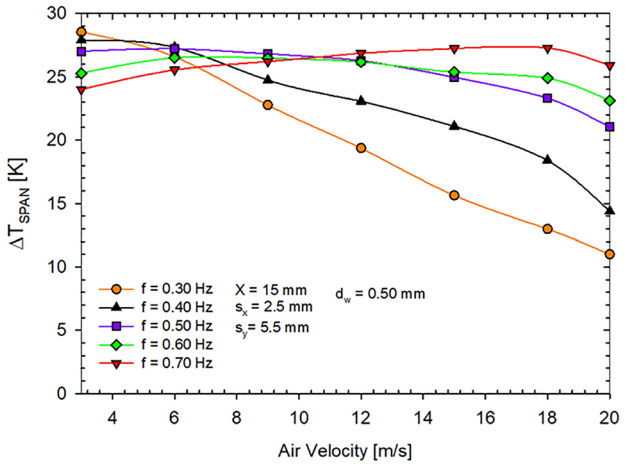

Fig. 4 Temperature span vs air velocity paramterized for cycle frequency

necessitating higher air velocity. Temperature variation exhibits an upward trend with frequency at higher speeds and a downward trend at lower speeds. Frequency variations also affect the time it takes for the fluid to pass through. At lower speeds, the temperature difference in the cold regenerator (ΔT_{COLD}) decreases with increasing frequency because the heat exchange mechanism is less effective, providing the fluid with more time to exchange heat with the wires. In contrast, at higher speeds, ΔT_{COLD} increases with frequency as the heat exchange mechanism becomes more effective. However, if the fluid passage time becomes excessively long, the driving force for the heat exchange process diminishes, leading to reduced heat exchange efficiency (Fig. 2).

The most significant air temperature variation detected reaches 13 K at 0.3 Hz and 6 m/s for cycle frequency and fluid velocity, respectively. A similar value of 12.5 K can be achieved at 0.7 Hz with a velocity of 18 m/s. Figure 3 illustrates the relationship between cooling power and velocity, taking cycle frequency into account. It is noteworthy that cooling power increases at high frequencies with air velocity because the mass flow rate of the fluid also increases. At low frequencies, cooling power initially rises, then reaches a maximum, and subsequently declines due to the decreasing ΔT_{COLD}. The variations in cooling power with frequency are less pronounced in the low-speed range. However, in the high-speed range, the increase in cooling power with frequency is more significant, primarily driven by the increase in ΔT_{COLD}. The most notable air temperature variation observed is 13 K, achieved at a cycle frequency of 0.3 Hz and a fluid velocity of 6 m/s. A similar temperature variation of 12.5 K can also be attained at 0.7 Hz with a velocity of 18 m/s. Figure 3 in the report depicts the relationship between cooling power and velocity, with cycle frequency taken into consideration. It is worth noting that cooling power increases at high frequencies as air velocity rises because the mass flow rate of the fluid also increases. At lower frequencies, cooling power initially rises, reaches a peak, and eventually declines due to the decreasing ΔT_{COLD}. The fluctuations in cooling power with frequency are less pronounced in the low-speed range. Conversely, in the high-speed range, the increase in cooling power with frequency is more significant, primarily attributable to the rise in ΔT. At high speeds and frequencies, notably promising cooling power values are achieved, which are suitable for macro-scale applications (greater than 1000 W). The maximum cooling power observed is 1320 W at 0.7 Hz and a velocity of 20 m/s. This achievement is particularly encouraging because it corresponds to a Specific Cooling Power (SCP) of 5700 W per kilogram, surpassing the performance of previously designed prototypes. Figure 4 illustrates the temperature span versus air velocity, with cycle frequency as a parameter. The graph demonstrates that the ΔT_{span} obtained

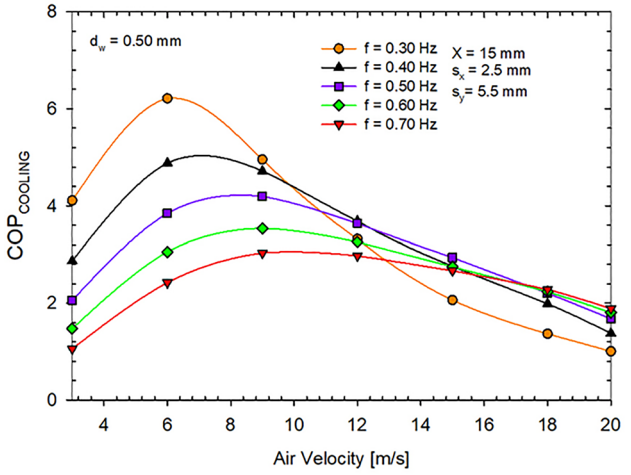

Fig. 5 COP as a function of air velocity for different cycle frequency values

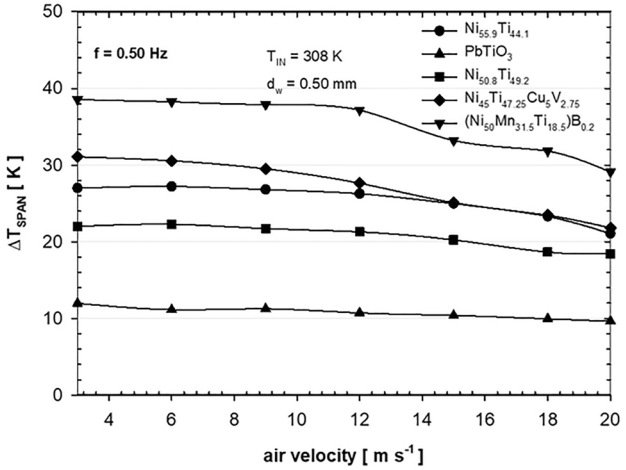

Fig. 6 Temperature span as a function of the air velocity for different eCMs

consistently exceeds 10 K, reaching its highest value of 28.5 K at a velocity of 3 m/s and a frequency of 0.3 Hz. The variation in the coefficient of performance (COP) concerning air flow velocity, with cycle frequency taken into account, is depicted in Fig. 5. The figure distinctly illustrates two distinct areas within the graph: one at low air speeds, ranging from 3 to 9 m/s, and another at high air speeds, from 9 to 20 m/s.

In the low-speed range, the COP increases as the frequency decreases. This pattern is a consequence of the more significant temperature variation that occurs in the cold regenerator at lower frequencies. Conversely, in the high-speed range, the cold-temperature variation diminishes at lower frequencies, along with the cooling power, resulting in a reduced COP for the same network. However, for each frequency, the COP ascends as the fluid velocity increases, reaching a peak before declining. The rise in pressure drops affects COP values at higher velocities, leading to increased power consumption coupled with the work of the fan. Therefore, it is not advisable to use a fluid velocity greater than 9 m/s.

Furthermore, it is noteworthy that the maximum COP value aligns with a higher speed as the cycle frequency increases. The highest COP of 6.22 is attained at a velocity of 6 m/s and a frequency of 0.3 Hz.

Materials Investigation

A comparison of various elastocaloric materials was conducted to determine the most suitable one for use in an experimental air conditioning device based on the elastocaloric effect. In these numerical simulations, the cycle frequency was held constant at 0.5 Hz, while the air velocity was varied within the range of 3 to 20 m/s.

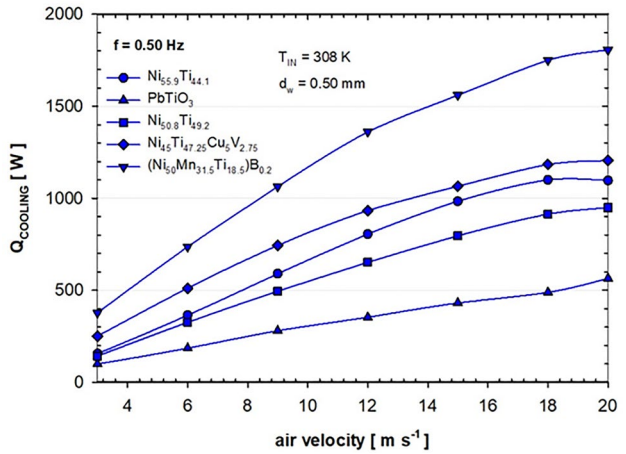

Fig. 7 Cooling power as a function of the air velocity for different eCMs

Figure 6 presents the temperature span of the device while varying air velocity. The figure demonstrates that the ΔTspan achievable with $(Ni_{50}Mn_{31.5}Ti_{18.5})_{99.8}B_{0.2}$ consistently exceeds 30 K, reaching its peak value of 38.6 K at a velocity of 3 m/s. When using $Ni_{45}Ti_{47.2}Cu_5V_{2.75}$, a ΔT_{span} greater than 30 K can be obtained within the lower range of air velocities. Figure 7 presents the cooling power of various materials as a function of velocity. Cooling power exhibits an increasing trend with air velocity since the fluid's mass flow rate also increases. With $(Ni_{50}Mn_{31.5}Ti_{18.5})_{99.8}B_{0.2}$, the cooling power at high velocities approaches nearly 2 kW. This value corresponds to a SCP of 7991 W per kilogram, surpassing the performance of previously designed prototypes. Cooling power values for $Ni_{55.9}Ti_{44.1}$ and $Ni_{45}Ti_{47.2}Cu_5V_{2.75}$ exceed 1 kW at high speeds. All $Q_{cooling}$ values exceeding 1 kW are suitable for constructing a prototype designed to

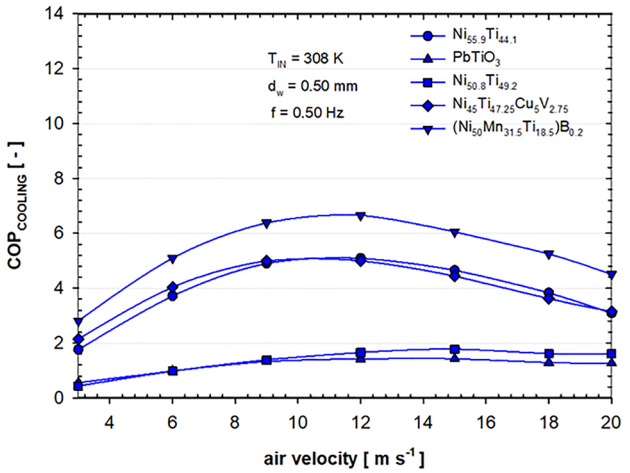

Fig. 8 COP as a function of the air velocity for different eCMs in cooling mode

operate in macro-scale applications. In Fig. 8, the COP values are presented in relation to air velocity. Across all materials, the COP exhibits a pattern of increasing with higher air velocities, reaching a peak before decreasing. The rise in pressure drops impacts COP values at higher velocities, leading to an increase in power consumption coupled with the fan's work. Consequently, it is not advisable to employ a fluid velocity greater than 12 m/s.

$(Ni_{50}Mn_{31.5}Ti_{18.5})_{99.8}B_{0.2}$ consistently displays higher COP values than all other materials across the entire range of air velocities. This is due to its elevated eCE (effective Coefficient of Performance), characterized by a high ΔT_{ad} and low w_{net} (network), indicating minimal hysteresis. The maximum COP of 6.66 is achieved at a velocity of 12 m/s. This value competes favorably with those attainable using conventional vapor compression heat pumps. COP values around 5 can be obtained for $Ni_{55.9}Ti_{44.1}$ and $Ni_{45}Ti_{47.2}Cu_5V_{2.75}$. However, COP values that are not competitive with conventional heat pumps are observed for $Ni_{50.8}Ti_{49.2}$ and $PbTiO_3$, with a maximum COP of 1.78 for $Ni_{50.8}Ti_{49.2}$ and 1.45 for $PbTiO_3$ at 15 m/s. This disparity can be attributed to $PbTiO_3$'s adiabatic temperature change falling within an unsuitable range for air conditioning applications. Conversely, the substantial hysteresis associated with $Ni_{50.8}Ti_{49.2}$ significantly impacts its energy performance negatively.

TEWI Analysis

To assess the environmental consequences of the elastocaloric system using the aforementioned elastocaloric materials and to make a comparative analysis with the TEWI (Total Equivalent Warming Impact) resulting from the vapor compression mono-split system, a percentage ratio called ΔTEWI is introduced as follows:

$$\frac{\Delta TEWI}{TEWI} = \frac{TEWI_{eCE} - TEWI_{VC}}{TEWI_{VC}} \tag{19}$$

Figure 9 displays the ΔTEWI resulting from the comparison, plotted against the airspeed. To compute the $CO_{(2,dir)}$ of the vapor compression system, a 5% annual leakage of HFC32 during regular operation was estimated. Conversely, the $CO_{(2,dir)}$ attributed to the elastocaloric heat pump consistently remains at zero under all conditions and for all materials tested, as the GWP (Global Warming Potential) of the eCMs is uniformly zero, considering their solid-state nature. Figure 9a illustrates the environmental impact in terms of the percentage ΔTEWI ratio pertaining to the cooling operation mode, while Fig. 9b depicts the environmental impact in terms of the percentage ΔTEWI ratio for the heating operation mode. Figures 9c and d offer a closer look at the negative portion of the ΔTEWI ratio, indicating less impact compared to vapor compression. The notable insight from the figures is that even though the direct contribution of the elastocaloric air device is consistently zero, it does not automatically guarantee a lower TEWI compared to the HFC32 vapor compression-based mono-split heat pump. The vapor compression heat pump is a mono-split inverter (A + +/A +) mounting 0.70 kg of HFC32 (GWP = 675) able to operate both in heat pumping and air conditioning modes (Model Riello AMW 25 ST). During winter mode the capacity at nominal air flow is 4.9 kW kg^{-1} and $COP_{hot} = 3.71$. During summer mode the capacity at nominal air flow is 3.7 kW kg^{-1} and $COP_{hot} = 3.23$. The annual energy consumptions are 839 kWh yr^{-1} (A +) and 147 kWh yr^{-1} (A + +), respectively, for the heat pump working in heating and cooling modes. Achieving a lower TEWI with the eCE system requires careful adjustment of operating conditions. Notably, as evident from Figs. 9(c) and 9(d), only $Ni_{55.92}Ti_{44.08}$ and $(Ni_{50}Mn_{31.5}Ti_{18.5})_{99.8}B_{0.2}$ exhibit a significant reduction in environmental impact in both heating and cooling modes. However, further exploration under additional operating points is necessary to establish a broader understanding of thermal responses and, consequently, environmental impacts.

Conclusion

In this work, a two-dimensional rotating numerical model of an elastocaloric refrigerator prototype has been presented. The aim of the numerical model was to optimize the operational parameters, the chemical composition of the elastocaloric material, and assess the environmental impact. The

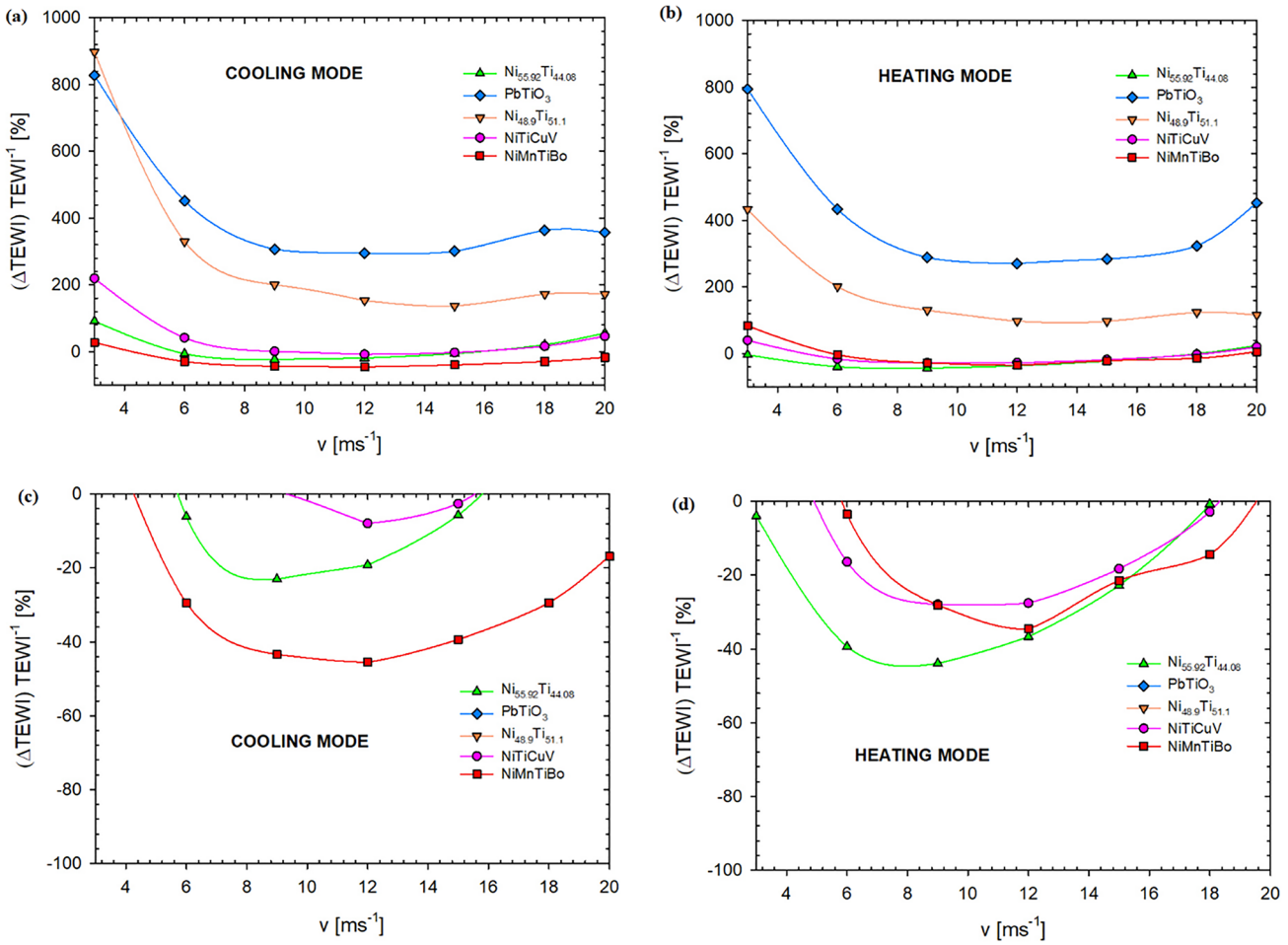

Fig. 9 ΔTEWI percentage vs airflow velocity of the device employing different elastocaloric materials as refrigerants during the **a** cooling and **b** heating operation modes

prototype is currently under development and involves the use of approximately 230 g of elastocaloric material. The conclusions of this study can be summarized as follows:

- There exists an optimal rotation frequency for each fluid velocity inside the device. It has been observed that as the air velocity increases, the temperature difference values decrease because the fluid does not have enough time to exchange heat with the elastocaloric material.
- The cooling power increases with higher velocity as the air flow rate increases. Furthermore, the cooling power decreases with lower rotation frequency and at high air velocity values.
- Two distinct regions can be observed in the COP graph: one at low air velocity values and another at high air velocity values. This trend is due to the fact that as the fluid velocity increases, the pressure drop inside the device also increases, which in turn requires more work to pump the fluid. The highest COP values occur at low frequencies (0.30 Hz) and in the region with low fluid velocity values.
- It has been verified that the chemical composition of the material has a significant impact on the thermal performance of the device. It has been demonstrated that Nitinol-based alloys exhibit higher values of temperature difference, cooling power, and COP.
- Quaternary alloys inside the device allow for higher COP and cooling power values compared to ternary and binary alloys. Therefore, in addition to providing durability advantages, they offer benefits in terms of temperature and performance coefficient.
- From an environmental perspective as well, quaternary alloys enable much lower values of ΔTEWI compared to vapor compression technology under specific operating conditions: air velocities between 8 and 15 m/s for all rotation frequencies.

Acknowledgements This research was funded through the project "SUSSTAINEBLE"—FISR2019 04798 granted by FISR – Fondo Integrativo Speciale per la Ricerca (Italian special supplementary fund for research).

Funding Open access funding provided by Università degli Studi di Napoli Federico II within the CRUI-CARE Agreement.

Data availability The data that support the findings of this study are available upon request. Please contact adriana.greco@unina.it for access to the data.

References

1. Silva DJ, Ventura J, Araújo JP (2021) Caloric devices: a review on numerical modeling and optimization strategies. Int J Energy Res 45(13):18498–18539. https://doi.org/10.1002/er.7023
2. Greco A, Aprea C, Maiorino A, Masselli C (2019) A review of the state of the art of solid-state caloric cooling processes at room-temperature before 2019. Int J Refrig 106:66–88. https://doi.org/10.1016/j.ijrefrig.2019.06.034
3. Torelló and E. Defay, (2021) Heat exchange law in caloric regenerators. Int J Refrig 127:174–179. https://doi.org/10.1016/j.ijrefrig.2021.02.024
4. Engelbrecht K (2019) Future prospects for elastocaloric devices. J Phys Energy. https://doi.org/10.1088/2515-7655/ab1573
5. Kabirifar P, Žerovnik A, Ahčin Ž, Porenta L, Brojan M, Tušek J (2019) Elastocaloric cooling: State-of-the-art and future challenges in designing regenerative elastocaloric devices. Strojniski Vestnik/Journal of Mechanical Engineering 65(11–12):615–630. https://doi.org/10.5545/sv-jme.2019.6369
6. Tušek J et al (2015) The Elastocaloric Effect: A Way to Cool Efficiently. Adv Energy Mater. https://doi.org/10.1002/aenm.201500361
7. Chen J, Lei L, Fang G (2015) Elastocaloric cooling of shape memory alloys: A review. Materials Today Communications. https://doi.org/10.1016/j.mtcomm.2021.102706
8. S. Nguyen et al (2022) Modeling the Steady-State Performance of SMA-based Elastocaloric Refrigeration Cycle, in InterSociety Conference on Thermal and Thermomechanical Phenomena in Electronic Systems, ITHERM, IEEE Computer Society. doi: https://doi.org/10.1109/iTherm54085.2022.9899645.
9. S. Qian et al (1979) High-performance multimode elastocaloric cooling system. Science. 380: 722–727. May 2023, [Online]. Available: https://www.science.org
10. He J, Ya C, Tang X, Ma L, Wu J, Lu B (2023) Numerical study of a cascade cycle for the reciprocating solid-state magnetic refrigerator. Appl Therm Eng. https://doi.org/10.1016/j.applthermaleng.2022.119695
11. Tomc U, Tušek J, Kitanovski A, Poredoš A (2013) A new magnetocaloric refrigeration principle with solid-state thermoelectric thermal diodes. Appl Therm Eng 58(1–2):1–10. https://doi.org/10.1016/j.applthermaleng.2013.03.063
12. Chen J, Zhang K, Kan Q, Yin H, Sun Q (2019) Ultra-high fatigue life of NiTi cylinders for compression-based elastocaloric cooling. Appl Phys Lett doi 10(1063/1):5115793
13. Qian S et al (2016) Design of a hydraulically driven compressive elastocaloric cooling system. Sci Technol Built Environ 22(5):500–506. https://doi.org/10.1080/23744731.2016.1171630
14. Zhao H, Wu K (2022) Experimental and numerical investigation of the transient thermal characteristics of twisted nitinol wires in a continuous torsional refrigeration system. PLoS ONE. https://doi.org/10.1371/journal.pone.0277415
15. Cirillo L, Greco A, Masselli C (2022) CHECK TEMPERATURE: A Small-Scale Elastocaloric Device for the Cooling of the Electronic Circuits. Int J Heat Technol 40(3):665–670. https://doi.org/10.18280/ijht.400302
16. Borzacchiello A, Cirillo L, Greco A, Masselli C (2023) A comparison between different materials with elastocaloric effect for a rotary cooling prototype. Appl Therm Eng 235:121344. https://doi.org/10.1016/J.APPLTHERMALENG.2023.121344
17. Cirillo L, Greco A, Masselli C (2023) Development of an electronic circuit cooling system using elastocaloric effect: a FEM comparison among different configurations. Appl Therm Eng. https://doi.org/10.1016/j.applthermaleng.2022.119463
18. Tušek J, Engelbrecht K, Mikkelsen LP, Pryds N (2015) Elastocaloric effect of Ni-Ti wire for application in a cooling device. J Appl Phys doi 10(1063/1):4913878
19. Aprea C, Greco A, Maiorino A, Masselli C (2017) A two-dimensional model of a solid-state regenerator based on combined electrocaloric–elastocaloric effect. Energy Procedia. https://doi.org/10.1016/j.egypro.2017.08.225
20. Cirillo L, Greco A, Masselli C (2023) A numerical comparison among different solutions for the design of a rotary elastocaloric prototype. Appl Therm Eng 228:120487. https://doi.org/10.1016/J.APPLTHERMALENG.2023.120487
21. Cirillo L, Greco A, Masselli C, Qian S (2022) A Preliminary Investigation on Designing of the Novel and First Italian elasto-Caloric Device". Int J Heat Technol 40(1):81–90. https://doi.org/10.18280/ijht.400110
22. Cirillo L, Greco A, Masselli C (2024) The energy performances of an elastocaloric device for air conditioning through numerical investigation. Appl Therm Eng 236:121517. https://doi.org/10.1016/J.APPLTHERMALENG.2023.121517
23. Cirillo L, Greco A, Masselli C, Qian S (2023) The Italian elastocaloric rotary air conditioner: Numerical modelling for optimal design and enhanced energy performances. Thermal Sci Eng Prog. https://doi.org/10.1016/j.tsep.2022.101605
24. Cui J et al (2012) Demonstration of high efficiency elastocaloric cooling with large Δt using NiTi wires. Appl Phys Lett doi 10(1063/1):4746257
25. Schmidt M, Schütze A, Seelecke S (2015) Scientific test setup for investigation of shape memory alloy based elastocaloric cooling processes. Int J Refrig 54:88–97. https://doi.org/10.1016/j.ijrefrig.2015.03.001
26. Qian S et al (2015) Performance enhancement of a compressive thermoelastic cooling system using multi-objective optimization and novel designs. Int J Refrigeration 57:62–76. https://doi.org/10.1016/j.ijrefrig.2015.04.012
27. Bruederlin F, Bumke L, Chluba C, Ossmer H, Quandt E, Kohl M (2018) Elastocaloric Cooling on the Miniature Scale: A Review on Materials and Device Engineering. Energy Technol 6(8):1588–1604. https://doi.org/10.1002/ente.201800137
28. Kilian Barthlomè, Efficient cooling and heating without harmful refrigerants.

29. Tušek J, Engelbrecht K, Eriksen D, Dall'Olio S, Tušek J, Pryds N (2016) A regenerative elastocaloric heat pump. Nat Energy 1:16134. https://doi.org/10.1038/nenergy.2016.134
30. H. Ossmer, S. Miyazaki, and M. Kohl (2015) Elastocaloric heat pumping using a shape memory alloy foil device," in 2015 Transducers - 2015 18th International Conference on Solid-State Sensors, Actuators and Microsystems, TRANSDUCERS 2015, Institute of Electrical and Electronics Engineers Inc., pp. 726–729. doi: https://doi.org/10.1109/TRANSDUCERS.2015.7181026.
31. S. M. Kirsch et al., "Continuous operating elastocaloric heating and cooling device: Air flow investigation and experimental parameter study," in ASME 2019 Conference on Smart Materials, Adaptive Structures and Intelligent Systems, SMASIS 2019, American Society of Mechanical Engineers (ASME), 2019. doi: https://doi.org/10.1115/SMASIS2019-5633.
32. Sharar DJ, Radice J, Warzoha R, Hanrahan B, Smith A (2021) Low-force elastocaloric refrigeration via bending. Appl Phys Lett doi 10(1063/5):0041500
33. Bruederlin F, Ossmer H, Wendler F, Miyazaki S, Kohl M (2017) SMA foil-based elastocaloric cooling: From material behavior to device engineering. J Phys D Appl Phys. https://doi.org/10.1088/1361-6463/aa87a2
34. Snodgrass R, Erickson D (2019) A multistage elastocaloric refrigerator and heat pump with 28 K temperature span. Sci Rep. https://doi.org/10.1038/s41598-019-54411-8
35. Sebald G, Komiya A, Jay J, Coativy G, Lebrun L (2020) Regenerative cooling using elastocaloric rubber: Analytical model and experiments. J Appl Phys doi 10(1063/1):5132361
36. Chen Y, Wang Y, Sun W, Qian S, Liu J (2022) A compact elastocaloric refrigerator. The Innovation. https://doi.org/10.1016/j.xinn.2022.100205
37. Li X, Cheng S, Sun Q (2022) A compact NiTi elastocaloric air cooler with low force bending actuation. Appl Therm Eng 215:118942. https://doi.org/10.1016/J.APPLTHERMALENG.2022.118942
38. Ianniciello L, Bartholomé K, Fitger A, Engelbrecht K (2022) Long life elastocaloric regenerator operating under compression. Appl Therm Eng 202:117838. https://doi.org/10.1016/J.APPLTHERMALENG.2021.117838